photonics

MDPI

Article

Tunable Optical Bistability and High-Sensitivity Terahertz Refractive-Index Sensing Based on a Fabry-Pérot Cavity Incorporating Weyl Semimetals

Shiqi Yang [1,†], Daohong Xiao [1,†], Jiaqi Ma [1], Bowen Wei [2], Kui Wang [3,4], Haishan Tian [1,*] and Leyong Jiang [1]

[1] School of Physics and Electronics, Hunan Normal University, Changsha 410081, China; 202330133052@hunnu.edu.cn (S.Y.); 202430133080@hunnu.edu.cn (D.X.); 202330133013@hunnu.edu.cn (J.M.); jiangly28@hunnu.edu.cn (L.J.)
[2] School of Mechanical Engineering, Jinan 250003, China; 202318161271@mail.sdu.edu.cn
[3] National Engineering and Technology Research Center for Emergency and Disaster Relief Equipment, PLA Joint Logistics Support Force University of Engineering, Chongqing 400033, China; kuiwang.nudt@hotmail.com
[4] Chongqing Gangli Environmental Protection Co., Ltd., Chongqing 400074, China
* Correspondence: tianhaishan@hunnu.edu.cn
† These authors contributed equally to this work.

Abstract

Optical bistability (OB) is a fundamental nonlinear effect enabling all-optical switching, logic, memory, and sensing, yet its practical implementation is often hindered by high power thresholds and limited tunability. Here, we theoretically demonstrate low-threshold and widely tunable OB in a Fabry-Pérot (FP) cavity integrated with a Weyl semimetal (WSM) layer. By combining the strong local-field enhancement of the FP cavity with the large third-order nonlinear conductivity of the WSM, we achieve pronounced bistable hysteresis loops in both the transmitted field amplitude and transmittance at terahertz frequencies, with incident field switching thresholds on the order of 10^6 V/m. The bistability thresholds and hysteresis width can be flexibly controlled by tuning the WSM Fermi energy, the position of the WSM layer inside the cavity, and the mirror transmittance. Moreover, exploiting the strong dependence of the down-switching threshold on small changes in the refractive index of the cavity medium, we propose a terahertz refractive-index sensor with a maximum sensitivity of 296.8 GW·m^{-2}·RIU^{-1}. These results provide a theoretical basis for tunable nonlinear photonic devices and threshold-based terahertz refractive-index sensors using topological semimetals.

Keywords: optical bistability; terahertz refractive-index sensor; Fabry-Pérot cavity; Weyl semimetals

Check for updates

Received: 27 June 2026
Revised: 6 August 2026
Accepted: 31 August 2026
Published: 1 September 2026

Copyright: © 2026 by the authors. Licensee MDPI, Basel, Switzerland. This article is an open access article distributed under the terms and conditions of the Creative Commons Attribution (CC BY) license.

1. Introduction

Optical bistability (OB) refers to a canonical nonlinear optical phenomenon wherein a system can exhibit two distinct, mutually switchable stable output states for a single given input state. A hallmark of OB is the presence of an S-shaped hysteresis loop in its input-output response curve [1]. As a typical nonlinear optical effect, OB has found widespread applications in a broad range of fields, including all-optical switches [2], optical logic gates [3], optical diodes [4], optical memories [5], and biosensors [6]. However, limited by the intrinsically low nonlinear coefficients of conventional materials, the realization of pronounced OB typically requires either large device footprints or high incident intensities.

This is fundamentally incompatible with the core requirements of modern photonic devices, namely a compact footprint and low power consumption. Consequently, conventional OB devices face substantial challenges for large-scale implementation in high-density photonic integrated circuits. To address this bottleneck, two main strategies have been pursued: designing micro- and nanostructures that enhance the local field and exploring materials with large third-order nonlinearities. At present, the requirements for the switching speed of all-optical bistable devices and optical switches in optical communication systems are not too high, so reducing the threshold switch power has become the main goal of research on optical bistable and all-optical switches. To date, various structures and mechanisms capable of achieving local field enhancement have been proposed, including Fabry-Pérot (FP) cavities [7], surface plasmons [8], photonic crystal cavities [9], topological edge states [10], and bound states in the continuum [11]. On the other hand, a variety of nonlinear materials with excellent optoelectronic properties have attracted extensive attention from the research community, such as graphene and three-dimensional Dirac semimetals [12], among which graphene-related research has been the most extensive. Recently, Wu et al. numerically investigated OB based on an asymmetric distributed Bragg reflector-graphene-Bragg reflector structure [13]. Eriksen et al. studied the generation and active manipulation of OB in two-level atoms adjacent to graphene sheets [14]. Ni et al. performed numerical simulation of OB in a periodic superconducting photonic multilayer structure incorporating graphene at cryogenic temperatures [15]. Despite its exceptional optoelectronic performance, graphene can be susceptible to thermal damage under high-power excitation [16]. Furthermore, for incident light in the terahertz band, graphene may require relatively high Fermi energies to achieve the desired response in the terahertz regime [17]. These drawbacks impose critical limitations on the development and practical application of graphene-based OB devices. Therefore, exploring OB phenomena and their underlying formation mechanisms in emerging novel materials remains a high-priority research direction in the field of optical bistability.

In recent years, Weyl semimetals (WSMs), a class of topological material with exceptional optoelectronic properties, have garnered extensive attention from the research community. WSMs possess a unique electronic structure, where the electronic states break either spatial inversion symmetry or time-reversal symmetry. Consequently, WSMs can exhibit pronounced nonreciprocal optical responses [18,19] without the application of an external magnetic field. Likewise, WSMs also demonstrate a variety of intriguing properties in the field of nonlinear optics. The singularity of the Berry flux field near the Weyl nodes of WSMs can drastically enhance topology-related nonlinear optical responses, including the bulk photovoltaic effect and the circular photogalvanic effect [20]. More recently, Zeng et al. adopted a lattice model beyond the linearized approximation, and revealed that the dominant source of the nonvanishing Berry curvature dipole in three-dimensional Weyl semimetal (WSM) is not the Weyl nodes themselves, but the contribution from the Fermi surface between the nodes [21]. Hu et al. experimentally demonstrated that the type-II WSM β-WP_2 exhibits a robust second-harmonic response unscreened by free electrons even under high electrical conductivity, which provides critical experimental support for the application of WSM in ultrafast topological nonlinear optoelectronic devices [22]. In the past few years, growing research efforts have been devoted to exploring the application potential of WSM in the field of OB. He et al. exploited the intrinsic nonreciprocity of WSM and structural resonant tunneling modes to realize tunable OB in the mid-infrared regime under zero external magnetic field [23]. Zhong et al. found that the third-order nonlinear conductivity of WSMs is much larger than that of traditional materials in long-wavelength bands such as the terahertz region [24]. These findings highlight the potential of WSM in

the development of novel optoelectronic devices and also leave broad scope for in-depth investigation and performance optimization in this research direction.

In this work, we theoretically investigate the OB behavior arising from the integration of a WSM layer into an FP cavity. By combining the strong nonlinear optical response of the WSM with the remarkable local-field enhancement of the FP cavity, we achieve low-threshold and tunable OB in the terahertz band. The switching threshold of the proposed structure is on the order of 10^6 V/m. Furthermore, the OB response curves can be flexibly tuned by adjusting the WSM Fermi energy, the position of the WSM layer, and the mirror transmission amplitude. Overall, these results provide a theoretical basis for using WSM-integrated FP cavities in tunable all-optical switching and threshold-based terahertz refractive-index sensing.

2. Theoretical Model and Method

We consider an FP cavity incorporating a single WSM layer. The FP cavity consists of two parallel mirrors separated by a fixed distance, with the WSM positioned at the cavity center and the remaining space of the cavity filled with air. It needs to be explained that these assumptions are mainly for illustrative purposes. In the actual case, the Weyl semimetal sheet can be sandwiched between two dielectric slabs. However, it should be noted that the introduction of the dielectric will lead to a significant increase in the threshold value. Nevertheless, it is not difficult to see that this scheme has a simple structure and does not require high preparation process requirements, making it competitive compared to previously reported optical bistable schemes. As shown in Figure 1, we take the z-axis to be normal to the mirror surfaces, with the x–y plane parallel to the layers. The cavity length L satisfies the resonance condition $2n_aL = m\lambda_0$, where n_a is the refractive index of air, λ_0 is the wavelength in a vacuum, and m is the resonance order (a positive integer). In this work, we set m = 12, corresponding to a cavity length $L = 300$ μm. The remaining parameters are set as follows: the thickness of the WSM $d_w = 1.03$ μm, the transmission amplitude of the mirrors ${t_m}^2 = 0.3$, and the incident angle $\theta = 0°$. Unlike the complex preparation process of Dirac materials such as graphene, many outer semimetals such as TaAs, TaP, etc., that have been theoretically calculated can be naturally synthesized without the need for detailed and complex control such as doping, which also brings convenience to material preparation. The incident optical field E_{in} is coupled into the structure from the left side, generating the corresponding reflected optical field E_r and transmitted optical field E_t. We focus on the relationship between the incident field E_{in} and the transmitted field E_t in this work.

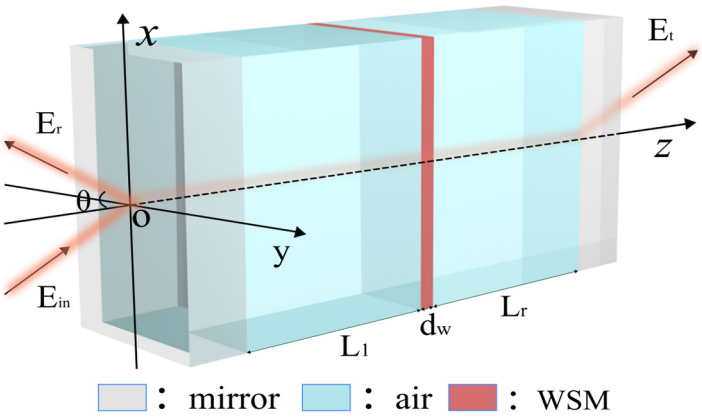


Figure 1. Schematic of an FP cavity incorporating a WSM layer. The incident light has an amplitude of E_{in}, and the amplitudes of the generated reflected and transmitted light are E_r and E_t, respectively.

Under low temperature and other conditions, the linear conductivity of the WSM is given by [25]:

$$\sigma^{(1)}(\omega) = \frac{e^2 v_F P_F^2 g_s g_\omega}{6\pi^2 \hbar^3 (\gamma - i\omega)}. \quad (1)$$

In Equation (1), the parameter g_s denotes the spin degeneracy factor, and g_ω denotes the Weyl node degeneracy factor. In this work, we set $g_s = 2$ and $g_\omega = 4$. e denotes the elementary charge, ω is the angular frequency of the incident light, γ is the electron relaxation rate, and $\hbar$ is the reduced Planck constant. E_F is the Fermi energy of the WSM, and the Fermi velocity $v_F = 10^6$ m/s. A higher v_F corresponds to a stronger coupling strength between carriers and the optical field. The parameter $P_F = E_F/v_F$ represents the magnitude of the Fermi momentum.

The WSM is assumed to be isotropic; therefore, its linear permittivity is given by [25]:

$$\varepsilon_1 = \varepsilon_b + \frac{i4\pi\sigma^{(1)}}{\varepsilon_0 \omega}. \quad (2)$$

In Equation (2), $\varepsilon_b = 10$ is the background dielectric constant, and ε_0 is the vacuum permittivity. It should be noted that "isotropy" is only a local approximation of the low-energy effective theory. The "isotropy" of WSM is a local property under specific theoretical approximations, not a macroscopic intrinsic property of the material.

The third-order nonlinear conductivity of the WSM is given by [25]:

$$\sigma^{(3)}(\omega) = \frac{e^4 v_F g_s g_\omega}{15\pi^2 \hbar^3 (-i\omega + \gamma)} \left[\frac{2}{(i\omega + \gamma)(-i\omega + \gamma)} + \frac{1}{(-i2\omega + \gamma)(-i\omega + \gamma)} \right]. \quad (3)$$

Here we set $\gamma = 0.005$ e/$\hbar$. The third-order nonlinear susceptibility of WSM is given by [25]:

$$\chi^{(3)} = \frac{i\sigma^{(3)}}{\varepsilon_0 \omega}. \quad (4)$$

It should be noted that in the subsequent OB calculation, due to the low threshold for OB occurrence, the influence of higher-order terms does not need to be considered here. The refractive index of the WSM can be written as the sum of the linear refractive index and the nonlinear refractive index [26]:

$$n_w = \sqrt{\varepsilon_1 + \chi^{(3)} |E_w|^2}. \quad (5)$$

In Equation (5), E_w denotes the local electric field inside the WSM layer and varies along the propagation direction. The calculation of E_w is detailed in the subsequent discussion.

It can be seen from Equations (4) and (5) that both $\chi^{(3)}$ and n_w of WSM are closely related to its linear and nonlinear conductivities. Therefore, by tuning parameters such as E_F and ω, we can flexibly modulate the OB response curve, thus realizing tunable OB.

For the layered structure, the transfer matrix method (TMM) is employed to investigate the relationship between the incident, transmitted, and reflected electric fields. We assume that the electromagnetic wave propagates along the z-axis, and all material layers and the mirrors are parallel to the x-y plane. First, for simplicity, we assume that the two mirrors are identical, with equal transmission and reflection coefficients. The transfer matrix M_m is used to relate the electromagnetic fields on the left and right sides of the mirror:

$$M_m = \frac{1}{|t_m|} \begin{pmatrix} 1 & i|r_m|Z_0 \\ \frac{-i|r_m|}{Z_0} & 1 \end{pmatrix}. \quad (6)$$

In Equation (6), $Z_0 = \sqrt{\mu_0/\varepsilon_0}$ is the wave impedance in a vacuum. $|t_m|$ and $|r_m|$ are the amplitude transmission and reflection coefficients of the mirror, respectively. For lossless mirrors, they satisfy $|t_m|^2 + |r_m|^2 = 1$.

https://doi.org/10.3390/photonics13090835

For a linear isotropic layer j, the transfer matrix under TE polarization is given by:

$$M_j = \begin{pmatrix} \cos\left(-k_{jz}d_j\right) & -i\sin(-k_{jz}d_j)/\eta_j \\ -i\eta_j\sin(-k_{jz}d_j) & \cos\left(-k_{jz}d_j\right) \end{pmatrix}. \quad (7)$$

In Equation (7), $k_{jz} = n_j\frac{w}{c}cos(\theta_j)$, and $\eta_j = \sqrt{\varepsilon_0/\mu_0}n_j\cos(\theta_j)$. n_j is the refractive index of the jth layer, θ_j is the angle of refraction, and d_j is the thickness of the layer. k_{jz} is the z-component of the wave vector in the jth layer, and η_j is the characteristic admittance of the TE-polarized wave in the jth layer. Equation (7) gives the general transfer matrix of a homogeneous layer and can be applied to both the air regions and the WSM sublayers by substituting the corresponding material parameters.

For an air region inside the FP cavity, Equation (7) is applied by setting $n_j = n_{\mathrm{a}}$, $d_j = d_{\mathrm{a}}$, $k_{jz} = k_{\mathrm{az}}$, and $\eta_j = \eta_{\mathrm{a}}$, where n_{a}, d_{a}, k_{az}, and η_{a} denote the refractive index, thickness, normal wave-vector component, and TE optical admittance of the corresponding air region, respectively. When the WSM layer is located at the cavity center, the air regions on its two sides have equal thicknesses. When the WSM layer is displaced from the center, the thicknesses of the left and right air regions are adjusted accordingly.

As indicated by Equation (5), the refractive index of the WSM depends on the local electric-field amplitude. Therefore, a single refractive-index value cannot be used to describe the entire nonlinear WSM layer directly. To account for the spatial variation in the local field, the WSM layer is divided into N equal sublayers, each with a thickness of $\Delta d_{\mathrm{w}} = d_{\mathrm{w}}/N$. When the sublayers are sufficiently thin, the electric field and refractive index within each sublayer can be approximated as uniform. We set $N = 100$. The calculation results indicate that the results at this point have highly converged. This also means that the value of n is sufficient to meet the current numerical calculation. The electric field at the right boundary of each sublayer is taken as the representative value of $E_{\mathrm{w},i}$ for that sublayer [26].

Accordingly, the transfer matrix $M_{\mathrm{w},i}$ of the ith WSM sublayer is obtained from Equation (7) by setting $n_j = n_{\mathrm{w},i}$, $d_j = \Delta d_{\mathrm{w}}$, $k_{jz} = k_{\mathrm{w},i,z}$, and $\eta_j = \eta_{\mathrm{w},i}$. Here, $n_{\mathrm{w},i} = n_{\mathrm{w}}(E_{\mathrm{w},i})$ is the local nonlinear refractive index determined by the electric-field amplitude $E_{\mathrm{w},i}$ in the ith sublayer, and $i = 1, 2,\ldots, N$.

The transfer matrix of the entire WSM layer is then given by the ordered product of the N sublayer transfer matrices:

$$M_W = M_{\mathrm{w},1}M_{\mathrm{w},2}M_{\mathrm{w},3}\ldots M_{\mathrm{w},N}. \quad (8)$$

The total transfer matrix M of the entire FP structure is obtained by cascading the transfer matrices of its constituent layers:

$$M = M_m M_a M_W M_a M_m. \quad (9)$$

Furthermore, the transmission coefficient of the whole structure can be calculated by the following formula:

$$t = \frac{(M_{11} + M_{12}\eta_r)\eta_l - (M_{21} + M_{22}\eta_r)}{(M_{11} + M_{12}\eta_r)\eta_l + (M_{21} + M_{22}\eta_r)}. \quad (10)$$

The reflection coefficient of the whole structure is as follows:

$$r = \frac{2\eta_l}{(M_{11} + M_{12}\eta_r)\eta_l + (M_{21} + M_{22}\eta_r)}. \quad (11)$$

In Equations (10) and (11), η_{l} and η_{r} are the characteristic admittances of the external environment in contact with the left and right sides of the structure, respectively.

The transmittance and reflectance of the structure are then obtained from the transmission and reflection coefficients:

$$R = |r|^2. \quad (12)$$

$$T = |t|^2. \tag{13}$$

Finally, the relationship between the incident, transmitted, and reflected electric fields can be expressed as:

$$|E_t| = |E_{in}| \times |t|. \tag{14}$$

$$|E_r| = |E_{in}| \times |r|. \tag{15}$$

3. Results and Discussion

In this section, we first examine how the insertion of the WSM layer modifies the transmittance and reflectance of the FP cavity. Compared with graphene, WSM has higher carrier mobility, higher Fermi velocity, easier preparation and stable performance. Meanwhile, WSM can also adjust the dielectric constant by changing the Fermi energy. Therefore, the high nonlinear refractive index of WSM is expected to play a crucial part in providing strong optical nonlinearity to realize low-threshold OB.

As described in Section 2, the transmittance and reflectance of the layered structure can be calculated using the TMM. To characterize the linear spectral response, we calculated the transmittance and reflectance spectra while neglecting the third-order nonlinear conductivity of the WSM, as shown in Figure 2.

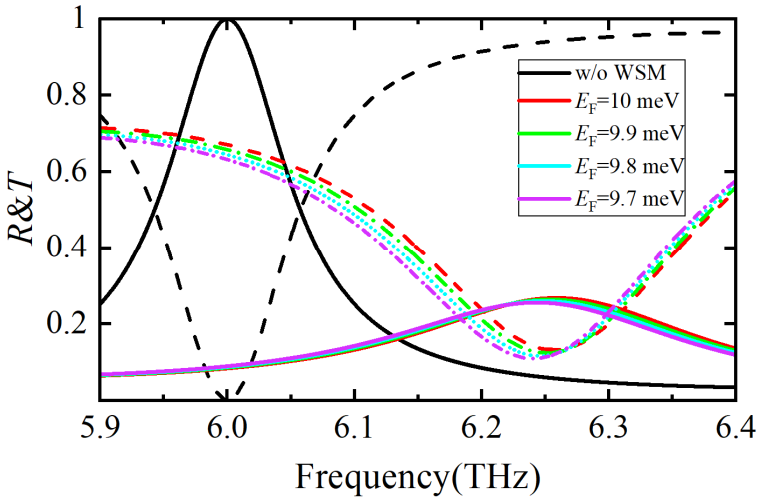


Figure 2. Transmittance (solid curves) and reflectance (dashed curves) as functions of frequency for different WSM Fermi energies.

In Figure 2, the solid lines represent the transmittance of the entire structure, while the dashed lines represent the reflectance. The black lines denote the transmittance and reflectance of the FP cavity without the inserted WSM layer. At 6 THz, the transmittance of the empty FP cavity approaches unity, indicating near-perfect transmission. This originates from the resonance effect of the FP cavity: when the wavelength satisfies the condition $2n_aL = m\lambda_0$, a stable standing wave field can be formed inside the cavity. However, after the introduction of the WSM layer, the spectral features of both the transmittance and reflectance shift significantly, and the peak intensities are also markedly reduced due to the optical absorption of the WSM.

Figure 2 also presents the variations in the transmittance and reflectance of the entire structure under different Fermi energies E_F. As E_F increases, the corresponding spectral features shift to higher frequencies, which is mainly attributed to the increase in the imaginary part of the linear conductivity $\sigma^{(1)}$ of the WSM. Therefore, effective modulation of the OB response curve can be realized by tuning the Fermi energy E_F of the WSM.

On this basis, we then investigate the nonlinear dependence of the transmittance and transmitted-field amplitude on the incident-field amplitude, as well as the influence of relevant parameters on the OB response curves. Based on the structural parameters at the FP cavity resonance, we fixed the operating frequency of the incident light at 6 THz, with all other parameters kept unchanged.

As described above, tuning the Fermi energy E_F of the WSM can effectively modulate the transmittance and reflectance of the entire structure. Therefore, using the slicing calculation method for the WSM described in Section 2, we plotted the relationship between the amplitude of the incident electric field $|E_{in}|$, the transmittance T of the composite structure, and the amplitude of the transmitted electric field $|E_t|$ under different E_F, as shown in Figure 3a,b.

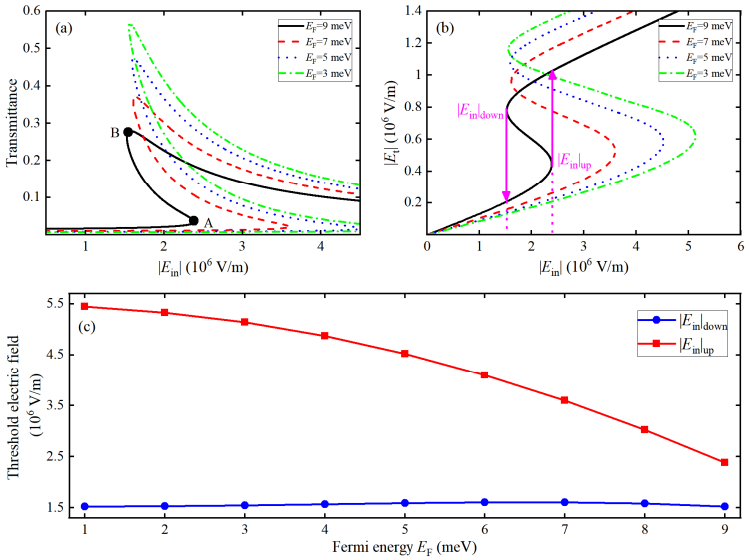


Figure 3. Effect of the WSM Fermi energy E_F on (**a**) transmittance bistability, (**b**) transmitted-field bistability, and (**c**) the upward and downward thresholds as functions of E_F.

The black solid curve in Figure 3a, corresponding to $E_F = 9$ meV, exhibits a typical S-shaped bistable response. At low incident-field amplitudes, T increases only slightly as $|E_{in}|$ increases. When $|E_{in}|$ increases to point A marked in Figure 3a, T exhibits an abrupt jump to a large value, followed by a slow decrease with the further growth of $|E_{in}|$. During the downward sweep of $|E_{in}|$, T first increases accordingly. Once $|E_{in}|$ drops to point B in Figure 3a, T undergoes an abrupt jump to a lower value. As shown in Figure 3b, the $|E_{in}|$ value corresponding to the upward jump is defined as the upward threshold of bistability $|E_{in}|_{up}$, and the value corresponding to the downward jump is defined as the downward threshold $|E_{in}|_{down}$. In OB, the middle branch of the S-curve itself is unstable. Therefore, only when the incident light intensity continues to increase or decrease will a transition from one "steady state" to another be achieved. Under this condition, the width of the hysteresis loop at $E_F = 9$ meV is calculated as $\Delta|E_{in}| = |E_{in}|_{up} - |E_{in}|_{down} = 0.86 \times 10^6$ V/m. It is not difficult to see that the threshold of this scheme can reach the order of 10^6 V/m, which has already reached the boundary of the low threshold.

It can be observed from Figure 3a,b that as E_F decreases from 9 to 7 meV, the upward threshold $|E_{in}|_{up}$ shifts towards a higher incident-field amplitude, while the downward threshold $|E_{in}|_{down}$ remains approximately unchanged. To more intuitively demonstrate the effect of E_F on the bistability thresholds, we plotted the variations of $|E_{in}|_{up}$ and $|E_{in}|_{down}$ with the Fermi energy E_F. As shown in Figure 3c, the width of the hysteresis loop $\Delta|E_{in}|$ decreases monotonically with the increase in E_F. Furthermore, a distinct OB phenomenon can hardly be observed when E_F exceeds 11 meV. This is mainly attributed to the fact that

the real part of the linear conductivity of the WSM increases significantly with the rise in E_F, which enhances the optical absorption of the incident light by the WSM. Therefore, in practical applications, flexible and convenient modulation of OB can be realized by tuning the Fermi energy of the WSM.

In practical device design, tuning the structure and relevant parameters of the FP cavity is also a critical approach for the modulation of OB. Therefore, in this work, we analyzed the influence of the position of the WSM layer within the FP cavity on the OB response curves. We define the displacement $\Delta z = 0$ μm when the WSM is located at the center of the FP cavity. Δz is positive when the WSM moves along the positive direction of the z-axis, and negative when it moves along the negative direction of the z-axis. On this basis, we fixed $E_F = 10$ meV and plotted the relationship between the amplitude of the incident electric field $|E_{in}|$, the transmittance T of the composite structure, and the amplitude of the transmitted electric field $|E_t|$ under different Δz, as shown in Figure 4a,b.

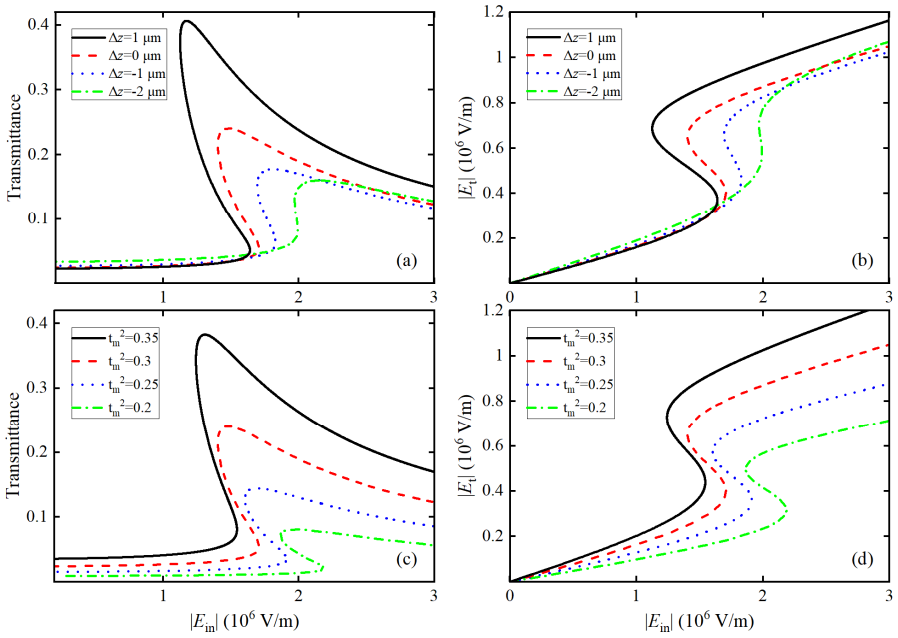


Figure 4. Effects of (**a**,**b**) the WSM displacement Δz and (**c**,**d**) the mirror power transmittance t_m^2 on (**a**,**c**) transmittance bistability and (**b**,**d**) transmitted-field bistability.

As can be seen from Figure 4a, with the movement of the WSM layer along the positive direction of the z-axis (increasing Δz), both the upward threshold $|E_{in}|_{up}$ and the downward threshold $|E_{in}|_{down}$ of OB decrease gradually, while the width of the hysteresis loop $\Delta|E_{in}|$ increases significantly. Meanwhile, the transmittance corresponding to the downward threshold also shows a marked enhancement. Figure 4b shows the same trend as Figure 4a. Furthermore, we find that as the displacement of the WSM layer along the negative direction of the z-axis increases, the S-shaped characteristic of the bistability gradually weakens until no distinct OB phenomenon can be observed. The underlying mechanism is that the slight displacement of the WSM layer modifies the distribution of the standing wave field inside the FP cavity, breaks the resonance condition, and thus significantly affects the generation and stability of the OB phenomenon in the proposed structure. On the other hand, the above results also confirm that adjusting the position of the WSM layer within the cavity is an effective approach for modulating the OB threshold.

On this basis, we also investigated the influence of the transmission amplitude of the FP cavity mirrors t_m on the OB threshold, as shown in Figure 4c,d. The results show that with the increase in t_m, both $|E_{in}|_{up}$ and $|E_{in}|_{down}$ decrease towards the low electric field regime, and the width of the hysteresis loop $\Delta|E_{in}|$ increases accordingly. It is worth noting

that although the variation in the above structural parameters leads to the change in the OB threshold, the threshold always maintains the same order of magnitude. These results provide guidance for selecting the WSM position and mirror transmittance in the design of OB devices.

Finally, we discuss the application of the WSM-integrated FP cavity structure in the field of terahertz refractive-index sensors. It is well established that sensitivity is the core performance metric of refractive-index sensors. During our theoretical investigation, we found that a small change in the refractive index of the cavity medium can induce a significant shift in the downward threshold $|E_{\mathrm{in}}|_{\mathrm{down}}$ of the OB curve, which provides a promising route for the design of high-sensitivity refractive-index sensors. We therefore consider a gas-filled terahertz refractive-index sensor in which the refractive-index change is inferred from the shift in the incident-field downward threshold. On this basis, the sensitivity S is defined as:

$$S = \frac{\Delta|E_{in}|_{down}}{\Delta n_a}. \tag{16}$$

In Equation (16), Δn_{a} is the change in the refractive index of the cavity medium, and $\Delta|E_{\mathrm{in}}|_{\mathrm{down}}$ is the corresponding shift in the downward threshold $|E_{\mathrm{in}}|_{\mathrm{down}}$ of the OB curve before and after the refractive index variation.

With all other parameters kept constant, we set the reference refractive index to $n_{\mathrm{a1}} = 1$, and the perturbed value to $n_{\mathrm{a2}} = 1.005$, giving $\Delta n_{\mathrm{a}} = n_{\mathrm{a2}} - n_{\mathrm{a1}} = 0.005$. As discussed in previous sections, the Fermi energy E_{F} plays a critical role in the modulation of the OB response curve. Because E_{F} controls the OB response, we next evaluate its effect on the threshold sensitivity S. We plotted the OB curves under different E_{F} and calculated the corresponding sensitivity S (in MV·m^{-1}·RIU^{-1}), as shown in Figure 5a–c. It can be observed that as E_{F} decreases from 10 meV to 8 meV, $\Delta|E_{\mathrm{in}}|_{\mathrm{down}}$ increases significantly. Correspondingly, the sensitivity S increases from 41.59 to 58.17 MV·m^{-1}·RIU^{-1}.

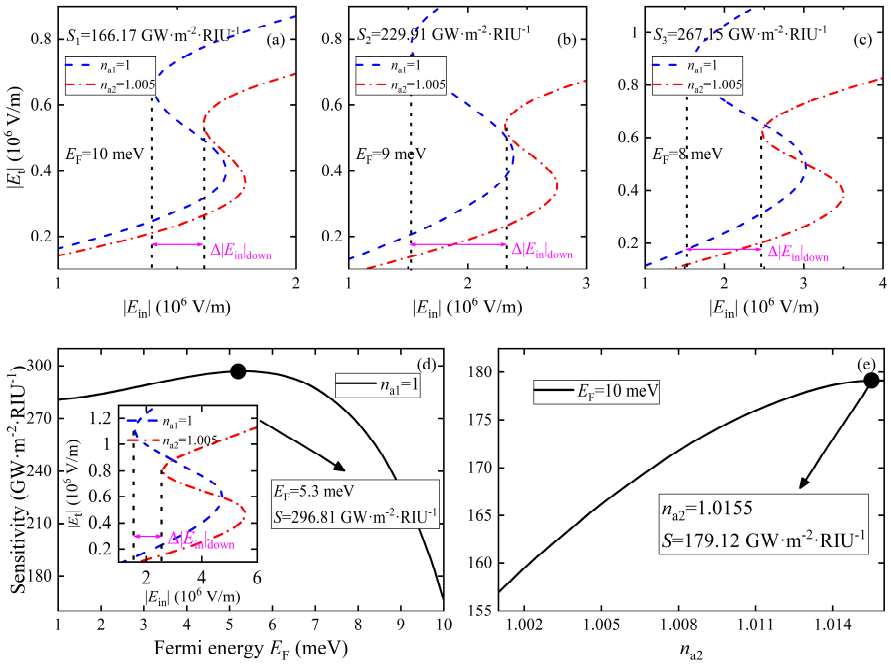


Figure 5. Transmitted-field amplitude versus incident-field amplitude at (**a**) E_{F} = 10 meV, (**b**) E_{F} = 9 meV, (**c**) E_{F} = 8 meV. (**d**) Threshold sensitivity S as a function of E_{F}. (**e**) Threshold sensitivity S as a function of the perturbed refractive index n_{a2} at E_{F} = 10 meV.

To more intuitively demonstrate the influence of E_{F} on S, we plotted the relationship between these two parameters, as shown in Figure 5d. With the increase in E_{F}, the

sensitivity S first shows a slow upward trend. The maximum S of 296.8 GW·m^{-2}·RIU^{-1} (63.92 MV·m^{-1}·RIU^{-1}) is achieved at E_F = 5.3 meV, with the corresponding OB curve shown in the inset of Figure 5d. As E_F increases further, the sensitivity S exhibits a sharp decrease. Furthermore, as established in the previous discussion, no distinct OB phenomenon can be observed when E_F exceeds 11 meV. Within the present model, lower E_F generally favors higher sensitivity. In fact, the fundamental carrier dynamics driving the enhanced real-part conductivity will more accurately capture the physical origin of this optical absorption. However, practical operation must account for temperature and the achievable precision of Fermi energy control.

In the field of terahertz sensing, most existing studies focus on the modulation law of device sensitivity by the variation in the baseline refractive index n_{a1} under a fixed refractive index variation Δn_a, while few studies have systematically investigated the influence mechanism of the amplitude of Δn_a on the sensing sensitivity under a fixed baseline refractive index n_{a1}.

Therefore, we plotted the curve of the sensitivity S as a function of the modified refractive index n_{a2}, as shown in Figure 5e. Here, E_F is fixed at 10 meV, and a variation trend similar to that in Figure 5d can be observed. The maximum sensitivity of 41.64 MV·m^{-1}·RIU^{-1} is obtained at n_{a2} = 1.003, i.e., a refractive index variation Δn_a = 0.003. Furthermore, it is found that when n_{a2} = 1.01, corresponding to Δn_a = 0.01, the sensitivity S reaches 40.89 MV·m^{-1}·RIU^{-1}. This result preliminarily reveals the potential value of the WSM-integrated FP cavity structure in enriching sensing application scenarios and broadening the quantitative detection range, which provides a critical reference for the practical development of this type of sensor. We have also take a quantitative comparison between the proposed sensor and existing OB-based or terahertz-based sensing platforms, as shown in Table 1. It is not difficult to see that this sensing scheme is competitive compared to existing reports.

Table 1. Comparison between different refractive index sensing schemes.

Ref.	Mechanism	Structure	Sensitivity	Frequency Range
[27]	Optical Tamm State	Graphene- Bragg reflector structure	407.36°/RIU	THz
[28]	Bloch surface wave sensor	Prism-photonic crystal structure	117°/RIU	THz
[29]	SPR sensor	Grating structure	237°/RIU	Near Infrared
[30]	Mode coupling sensor	Graphene–Bragg reflector structure (with defect layer)	1085°/RIU	THz
[31]	Cavity resonance	Graphene–Bragg Photonic Crystal FP Cavity	96.48 × 10^5 V/m·RIU	THz
This work	FP cavity nonlinearity	WSM-FP cavity	63.92 MV·m^{-1}·RIU^{-1}	THz

4. Conclusions

In summary, we have theoretically investigated low-threshold and tunable OB in a WSM-integrated FP cavity structure, as well as its application potential as a terahertz refractive-index sensor. Leveraging the local field enhancement effect of the FP cavity and the large third-order nonlinear conductivity of the WSM, we have theoretically demonstrated

OB in both the transmitted electric field amplitude and the transmittance of the proposed structure. By tuning the Fermi energy E_F of the WSM, adjusting the position of the WSM layer within the FP cavity, and modifying the transmission amplitude of the cavity mirrors, we can flexibly modulate the upward and downward thresholds of OB, as well as the width of the hysteresis loop. Furthermore, based on the high sensitivity of the structure to the refractive index variation in the cavity medium inside the cavity, we can realize a refractive-index sensor with high sensitivity and a wide tunable range. It is anticipated that the WSM-integrated FP cavity structure will exhibit promising application prospects in the fields of nonlinear optoelectronic devices and high-performance refractive-index sensors.

Author Contributions: S.Y. undertook the writing of the manuscript, completed the formula derivation and data collection with D.X. and J.M., and performed the numerical calculations with the help of B.W. and K.W. L.J. and H.T. participated in the conception and design of the work, and critically revised the theoretical model and methodology. All authors have read and agreed to the published version of the manuscript.

Funding: This work was supported by the National Natural Science Foundation of China (Grant No. 62375084), Natural Science Foundation of Hunan Province (Grant No. 2025JJ50055), Scientific Research Fund of Hunan Provincial Education Department (Grant No. 24A0050), and Chongqing Municipal Natural Science Foundation (CSTB2022NSCQ-MSX0192).

Data Availability Statement: The data that support the findings of this study are available from the corresponding author upon reasonable request.

Conflicts of Interest: Author Kui Wang is the employee of Chongqing Gangli Environmental Protection Co., Ltd. The authors declare no conflict of interest.

References

1. Gibbs, H.M. *Optical Bistability: Controlling Light with Light*, 1st ed.; Academic Press: New York, NY, USA, 1985; p. 471.
2. Liu, J.C.; Wang, F.L.; Han, J.Y.; Hao, Y.Z.; Yang, Y.D.; Xiao, J.L.; Huang, Y.Z. All-Optical Switching and Multiple Logic Gates Based on Hybrid Square–Rectangular Laser. *J. Light. Technol.* **2020**, *38*, 1382–1390. [CrossRef]
3. Zhang, W.L.; Jiang, Y.; Zhu, Y.Y.; Wang, F.; Rao, Y.J. All-optical bistable logic control based on coupled Tamm plasmons. *Opt. Lett.* **2013**, *38*, 4092–4095. [CrossRef] [PubMed]
4. Xia, X.-W.; Zhang, X.-Q.; Xu, J.-P.; Yang, Y.-P. High contrast all-optical diode based on direction-dependent optical bistability within asymmetric ring cavity. *Chin. Phys. B* **2016**, *25*, 084211. [CrossRef]
5. Kim, J.S.; Ri, C.S.; Yun, Y.J.; Im, S.J.; Kim, K.D.; Song, K.S.; Pae, J.S.; Ho, K.S. On-chip deep subwavelength optomagnetic bistable memory based on inverse Faraday effect related nonlinearity in graphene waveguide ring resonators. *Phys. Rev. B* **2024**, *110*, 195421. [CrossRef]
6. Li, J.-B.; Liang, S.; Xiao, S.; He, M.-D.; Liu, L.-H.; Luo, J.-H.; Chen, L.-Q. A sensitive biosensor based on optical bistability in a semiconductor quantum dot-DNA nanohybrid. *J. Phys. D. Appl. Phys.* **2019**, *52*, 035401. [CrossRef]
7. Protsenko, I.E.; Uskov, A.V. Single-photon optical bistability in a small nonlinear cavity. *Phys. Rev. A* **2023**, *108*, 023724. [CrossRef]
8. Hu, H.T.; Alvarez-Pérez, G.; Otomalo, T.O.; Ciracì, C. Low-Power Threshold Optical Bistability Enabled by Hydrodynamic Kerr Nonlinearity of Free Carriers in Heavily Doped Semiconductors. *ACS Photonics* **2024**, *11*, 4812–4817. [CrossRef] [PubMed]
9. Yang, Y.Q.; Zhang, T.Y.; Yan, J.Y.; Li, P.G.; Li, Z.T. Topologically-protected optical bistability based on two-dimensional photonic crystal L6 nanocavity dimer array. *Opt. Express* **2024**, *32*, 28462–28471. [CrossRef] [PubMed]
10. Wang, J.X.; Li, X.X.; Chen, Y.H.; Yin, H.X.; Sun, Y.F.; Zhang, X.D. Bistable optical memory using topological cavity-edge waveguide composite structure. *Opt. Commun.* **2024**, *558*, 130370. [CrossRef]
11. Wang, W.J.; Liang, S.J.; Huo, Y.Y.; Yue, Q.Y.; Cai, Y.J.; Ning, T.Y. Ultra-low threshold optical bistability assisted by merging bound states in the continuum. *Opt. Express* **2025**, *33*, 44608–44621. [CrossRef] [PubMed]
12. Wu, X.H.; Guo, Y.Y.; Long, X.; Wang, Q.K. Nonlinear Optical Bistability Based on Surface Plasmons with Nonlinear Dirac Semimetal Substrate. *Coatings* **2024**, *14*, 394. [CrossRef]
13. Wu, Y.X.; Zhao, X.J.; Hu, J.S.; Xu, H.L. Low threshold optical bistability based on coupled graphene Tamm states. *Results Phys.* **2021**, *21*, 103824. [CrossRef]
14. Eriksen, M.H.; Olsen, J.E.; Wolff, C.; Cox, J.D. Optoelectronic Control of Atomic Bistability with Graphene. *Phys. Rev. Lett.* **2022**, *129*, 253602. [CrossRef] [PubMed]

15. Ni, H.; Zhou, G.P.; Xu, S.L.; Liu, F.H.; Zhao, M.M.; Duan, S.R.; Zhao, D. Low-temperature optical bistability and multistability in superconducting photonic multilayers with graphene. *Results Phys.* **2023**, *52*, 106867. [CrossRef]
16. Chen, H.; Wang, C.; Ouyang, H.; Song, Y.; Jiang, T. All-optical modulation with 2D layered materials: Status and prospects. *Nanophotonics* **2020**, *9*, 2107–2124. [CrossRef]
17. Choi, H.J.; Baek, I.H.; Kang, B.J.; Kim, H.D.; Oh, S.S.; Hamm, J.M.; Pusch, A.; Park, J.; Lee, K.; Son, J.; et al. Control of terahertz nonlinear transmission with electrically gated graphene metadevices. *Sci. Rep.* **2017**, *7*, 42833. [CrossRef] [PubMed]
18. Guo, C.; Asadchy, V.S.; Zhao, B.; Fan, S. Light control with Weyl semimetals. *eLight* **2023**, *3*, 2. [CrossRef]
19. Xu, H.-R.; Guo, C.-M.; Li, X.; Zhang, H.-F. Implementation of Unilateral thermal nonreciprocity and front and rear electromagnetic nonreciprocity based on Weyl semimetal. *Opt. Mater.* **2024**, *150*, 115134. [CrossRef]
20. Weng, H. Lighting up Weyl semimetals. *Nat. Mater.* **2019**, *18*, 428–429. [CrossRef] [PubMed]
21. Zeng, C.A.C.; Nandy, S.; Tewari, S. Nonlinear transport in Weyl semimetals induced by Berry curvature dipole. *Phys. Rev. B* **2021**, *103*, 245119. [CrossRef]
22. Hu, T.C.; Su, B.; Shi, L.Y.; Wang, Z.X.; Yue, L.; Xu, S.X.; Zhang, S.J.; Liu, Q.M.; Wu, Q.; Li, R.S.; et al. Strong Nonlinear Optical Response and Transient Symmetry Switch in Type-II Weyl Semimetal β-WP_2. *Adv. Opt. Mater.* **2023**, *11*, 2202639. [CrossRef]
23. He, M.; Wu, F.; Yin, C. Non-reciprocal optical bistability of sandwiched structure containing magnetic Weyl semimetals. *Phys. B Condens. Matter* **2024**, *688*, 416171. [CrossRef]
24. Zhong, Y.; Feng, W.; Liu, Z.; Zhang, C.; Cao, J.C. Nonlinear optical conductivity of Weyl semimetals in the terahertz regime. *Phys. B Condens. Matter* **2019**, *555*, 81–84. [CrossRef]
25. Almutairi, S.; Chen, Q.; Tokman, M.; Belyanin, A. Four-wave mixing in Weyl semimetals. *Phys. Rev. B* **2020**, *101*, 235156. [CrossRef]
26. He, M.; Li, T.; Huo, K.; Zhang, J.; Wu, F.; Yin, C. Low-threshold bistable absorption in asymmetrical one-dimensional photonic crystals containing Weyl semimetal defects. *Eur. Phys. J. B* **2023**, *96*, 128. [CrossRef]
27. Tang, J.; Ye, Y.Y.; Xu, J.; Zheng, Z.W.; Jin, X.L.; Jiang, L.Y.; Jiang, J.; Xiang, Y.J. High-Sensitivity Terahertz Refractive Index Sensor in a Multilayered Structure with Graphene. *Nanomaterials* **2020**, *10*, 500. [CrossRef] [PubMed]
28. Baghbadorani, H.K.; Barvestani, J.; Entezar, S.R. Biosensors based on Bloch surface waves in one-dimensional photonic crystal with graphene nanolayers. *Appl. Opt.* **2017**, *58*, 462–469. [CrossRef] [PubMed]
29. Cai, D.; Lu, Y.; Lin, K.; Wang, P.; Ming, H. Improving the sensitivity of SPR sensors based on gratings by double-dips method (DDM). *Opt. Express* **2008**, *16*, 14597–14602. [CrossRef] [PubMed]
30. Liu, Y.M.; Zheng, Q.W.; Yuan, H.X.; Wang, S.P.; Yin, K.Q.; Dai, X.Y.; Zou, X.; Jiang, L.Y. High Sensitivity Terahertz Biosensor Based on Mode Coupling of a Graphene/Bragg Reflector Hybrid Structure. *Biosensors* **2021**, *11*, 377. [CrossRef] [PubMed]
31. Yang, S.Q.; Xiao, D.H.; Luo, X.J.; Wang, K.; Tian, H.S.; Jiang, L.Y. High-Sensitivity Bistable Biosensor Based on the Photonic Crystal Fabry-Pérot Cavity with Weyl Semimetal. *Photonics* **2026**, *13*, 716. [CrossRef]

Disclaimer/Publisher's Note: The statements, opinions and data contained in all publications are solely those of the individual author(s) and contributor(s) and not of MDPI and/or the editor(s). MDPI and/or the editor(s) disclaim responsibility for any injury to people or property resulting from any ideas, methods, instructions or products referred to in the content.